applied sciences

MDPI

Article

Silicon-Based Multilayer Waveguides for Integrated Photonic Devices from the Near to Mid Infrared

Iñaki López García [1], Mario Siciliani de Cumis [2,*], Davide Mazzotti [1], Iacopo Galli [1], Pablo Cancio Pastor [1] and Paolo De Natale [1]

[1] CNR-INO & LENS, Via Carrara 1, 50019 Sesto Fiorentino, Italy; inaki.lopez@outlook.com (I.L.G.); davide.mazzotti@ino.cnr.it (D.M.); iacopo.galli@ino.cnr.it (I.G.); pablo.canciopastor@ino.cnr.it (P.C.P.); paolo.denatale@ino.cnr.it (P.D.N.)

[2] ASI Agenzia Spaziale Italiana–Centro di Geodesia Spaziale, Località Terleccchia, 75100 Matera, Italy

* Correspondence: mario.sicilianidecumis@asi.it

Abstract: Advancements in spectroscopy, quantum optics, communication, and sensing require new classes of integrated photonic devices to host a wide range of non-linear optical processes involving wavelengths from the visible to the infrared. In this framework, waveguide (WG) structures designed with innovative geometry and materials can play a key role. We report both finite element modeling and experimental characterization of silicon nitride multilayer WGs from the visible to the mid-infrared spectral regions. The simulations evaluated optical behavior and mechanical stress as a function of number of WG layers and photonic structure dimensions. WGs were optimized for waveguiding at 1550 nm and 2640 nm. Experimental characterization focused on optical behavior and coupling losses from 532 nm to 2640 nm. Measured losses in WGs indicate a quasi-perfect waveguiding behavior in the IR range (with losses below 6 dB), with a relevant increase (up to 20 dB) in the visible range.

Keywords: non-linear optics; finite element modeling; multilayer waveguide; silicon nitride; mid infrared spectroscopy; photonic devices

check for updates

Citation: García, Ia.Lp.; Siciliani de Cumis, M.; Mazzotti, D.; Galli, I.; Cancio Pastor, P.; De Natale, P. Silicon-Based Multilayer Waveguides for Integrated Photonic Devices from the Near to Mid Infrared. *Appl. Sci.* **2021**, *11*, 1227. https://doi.org/10.3390/app11031227

Academic Editor: Costantino De Angelis

Received: 2 December 2020

Accepted: 25 January 2021

Published: 29 January 2021

Publisher's Note: MDPI stays neutral with regard to jurisdictional claims in published maps and institutional affiliations.

Copyright: © 2021 by the authors. Licensee MDPI, Basel, Switzerland. This article is an open access article distributed under the terms and conditions of the Creative Commons Attribution (CC BY) license (https://creativecommons.org/licenses/by/4.0/).

1. Introduction

In the last few years, Quantum Technologies have been recognized as key for novel disruptive instruments and future industrial products, with the prospect to become pervasive in all application areas, as well as in everyday life [1–3]. This "second quantum revolution" will need miniaturized photonic platforms to be embedded in newly designed instruments and products. Therefore, novel laser configurations and photonic components will underpin such developments [4,5] in every spectral region, from the UV to the far infrared [6,7]. In this context, mid-infrared (MIR) can play a key role. Indeed, this is the so-called fingerprint region, already crucial for a number of civilian as well as defense and security applications: from spectroscopy [8–10] to free-space communication [11,12], from metrology to imaging [13–16], and from photonics [17–21] to quantum technologies [22]. In particular, waveguide WG devices are very important for photonics, communication, and health applications [7,20–24]. MIR WG structures come in a number of geometric shapes and materials, e.g., GaAs/AlGaAs, III-V/silicon, silicon-on-insulator (SOI), silicon-on-sapphire, silicon, silicon-on-nitride, silicon-on-calcium-fluoride, silicon-on-lithium-niobate, germanium-on-silicon, or germanium-on-silicon-nitride platforms [18,25–28]. However, MIR optical components (detectors, fibers, waveplates, polarizers, optical isolators, etc.) are generally less efficient and have higher production costs than their counterparts in the near infrared (NIR). In this context, it would be desirable to have very broadband WGs working from the MIR to the NIR/visible region. In order to have an integrated platform with components working from visible to MIR, the use of non-linear frequency conversion processes based on silicon is crucial, and exploits the advantages of a well-established technology,

providing scalability and cost reduction. In particular, the latest studies report non-linear frequency up-conversion in quasi-phase-matched (QPM) Si-based WGs [27–35], particularly second-harmonic generation (SHG) and sum-frequency generation (SFG) [36,37]. Recent experiments with Si-based devices reported non-linear generation with output powers above the nW range [38–40]. In other recent studies, silicon nitride (Si_3N_4) was used for SHG [41], although with an efficiency of about two orders of magnitude lower than in traditional non-linear crystals. It is well known that Si_3N_4 is a centrosymmetric material, therefore lacking any bulk second-order non-linearity; it is nevertheless observed in Si_3N_4 or Si_xN_y thin films [42–44]. Another well-known possibility with $Si_3N_4$is to strain silicon WGs, thus enhancing the non-linear response [31,45,46], but in this case the non-linearity is mostly due to the silicon itself [47,48]. To date, an extremely small $\chi^{(2)}$ coefficient in integrated platforms is attributed to the presence of an asymmetric dipole potential at the interface between the two materials (i.e., Si_3N_4 and SiO_2). In this way, it is possible to break the center-symmetry of the two materials in a limited spatial region [41]. In previous studies, large propagation losses were reported [49]. This was explained by poor optical confinement of guided modes, due to a WG core thickness that was too small. In particular, the large strain occurring between the core and the cladding layers limits the thickness value [40,50].

One of the targets of this study is the evaluation of the optical properties of waveguiding structures in different spectral regions. This is the first step to enabling non-linear processes. Indeed, to host these processes, a platform is needed that would be capable of guiding a wider range of wavelengths. The following steps are a WG design optimizing phase matching and using opportune materials to enhance the desired non-linear processes.

In the present study, we improve optical confinement by testing non-stoichiometric Si_xN_y/SiO_2 multilayer WGs (hereafter, we refer to the layer material as SiN). These devices were fabricated and provided by the Bruno Kessler Foundation (FBK) and the University of Trento. The presence of intermediate, thin SiO_2 layers was used to reduce the tensile stress fraction of the overall stress acting on the WG. Thus, a WG core with a total SiN thickness larger than the critical one could be obtained. Our study is divided into two parts: In the first part, we perform a finite element modeling (FEM) of multilayer structure WGs focused on waveguiding behavior in the telecom range to host non-linear optical processes; in the second part, we carry out an initial optical characterization of WGs built according to the theoretical modeling.

2. Materials and Methods

2.1. Geometry and Simulations

We explored a geometry based on non-stoichiometric silicon nitride (SiN) in combination with silicon dioxide (SiO_2) (Figure 1). This choice is motivated by the need to have both a refractive index larger than that of SiO_2 (2.35 vs. 1.46) [48,51], resulting in smaller waveguide dimensions, and a large energy bandgap (close to 5 eV), resulting in lower material losses [44] and the absence of a two-photon absorption (TPA) in the NIR/MIR. We performed two kinds of simulations for the WGs:

1. Optical WG behavior from 500 nm to 4000 nm, in order to optimize waveguiding at 1.5 μm and 2.5–3.1 μm (crucial for environmental monitoring and quantum processes [52,53]).
2. Mechanical stress in the multilayer structure. The implications of these simulations concerned possible local second-order non-linearities of such devices. For this study, a superficial charge was applied at layer interfaces, according to the number of layers. The Young's modulus, Poisson coefficient, and density were fixed to values from the relevant literature [54]. The results are given in the next paragraphs.

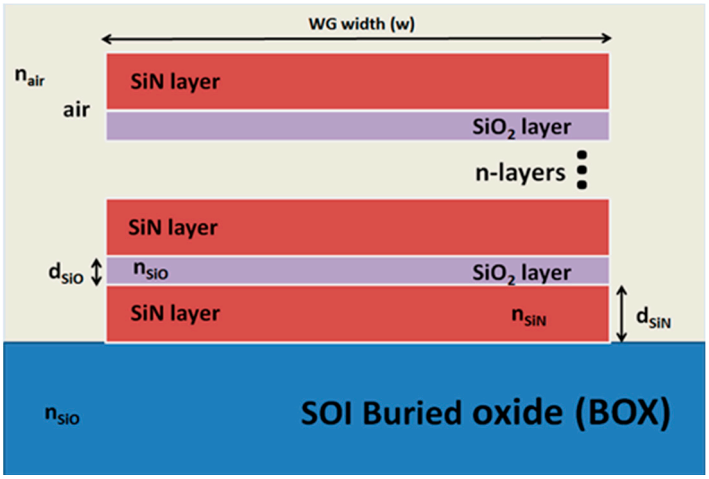

Figure 1. Cross section of the Waveguided model comprising some SiN/SiO_2 layers. During the simulation, we changed the number of layers, layer width (w), and layer thickness (dSiO, dSiN).

Waveguides were fabricated by FBK in order to carry out an initial evaluation of their properties. We investigated the losses experienced along the multilayer WG, measuring the transmitted power value at one WG end.

2.2. Experimental Setup

Figure 2 shows the free-space optical setup used for the characterization of the WGs provided by FBK and the University of Trento. The samples available for measurement had a common thickness size (770 nm), with a length of 6 mm and five different widths (7, 8.3, 8.6, 9.4, and 10 µm—see also the last figure for info about stress for every sample). The goal of this experiment was an initial evaluation of the WG properties (measuring the transmitted power value at one WG end) at different wavelengths and to compare those results with the FEM analysis described in next sections.

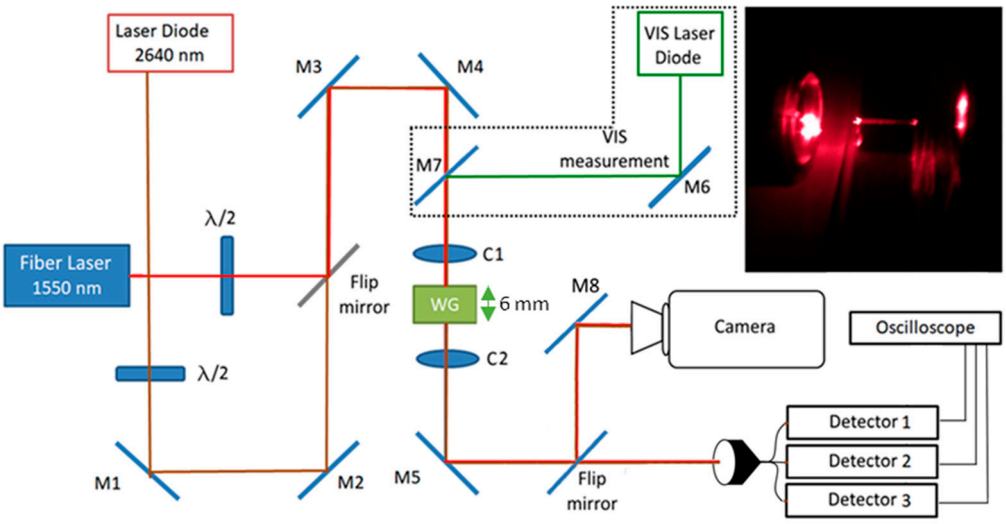

Figure 2. Schematic of the free-space optical system assembly for the characterization of the waveguiding behaviour (in text and figure, M is for mirror and C is for collimator). Inset: Optical pictures of behaviour at 635 nm of a 6 mm-length WG with a width of 9 µm.

We used four different laser sources to monitor the waveguiding behavior from the visible to the MIR range: a laser diode emitting 0.9 mW at 532 nm (Thorlabs CPS532), a

laser diode with 1.2 mW of power at 635 nm (Thorlabs CPS635), an Er-doped fiber laser with 0.8 W at 1550 nm (IPG Photonics), and a DFB laser with 7 mW at 2640 nm (Nanoplus).

Our experimental setup (Figure 2) enabled a fast switch of the different sources and detectors. Flip mirrors were used to easily switch between visible (M7) and IR (flip mirror) input light in the tested WGs. The remaining propagation optics, except WG-input and WG-output collimators were shared at all tested wavelengths by using gold-coated mirrors. For the collimation optics (C1 and C2 in the figure), a couple of collimation lenses were used, anti-reflective coated between 350 and 700 nm for the visible sources and between 1.6 and 3 μm for the IR sources. Input laser beams at the different wavelengths were optically shaped to match the WG' mode field diameters. In Figure 2 lines of different colors are depicted according to the different spectral regions: visible (green line), NIR (red line), and MIR (brown line). Half-wave plates were placed in the NIR and MIR lasers' input paths in order to control beam polarization. Fine realignment of the input and output optics to optimize waveguiding and detection was performed when switching between laser sources.

At the WG output, the light was sent to three different detectors, depending on the source in use. In addition, to analyze, check, and optimize the waveguiding behavior of the samples, as well as to control the correct IR beam line-up, an additional branch could be selected, by means of the flip mirror, after M5 to send the output light to a charge-coupled device (CCD) camera (an Si sensor for visible light, and an InSb camera for NIR/MIR light).

3. Results

3.1. Modeling

3.1.1. Optical Modeling

In order to guide a wide range of wavelengths from visible to IR, a SiN multilayer WG structure was designed to guide those and host non-linear optical processes between a TEM-polarized pump and signal modes with NIR–MIR wavelengths. The basic WG structure that was studied is shown in Figure 1. The refractive indexes of SiO_2, SiN, and air were found in the relevant literature [55,56].

We changed the WG dimensions and number of layers to optimize the waveguiding behavior in a wide emission spectrum range, as well as to host the non-linear optical process involving NIR and MIR wavelengths. The cross-section dimension of the surrounding air was selected according to WG dimensions; the distance between the WG edge and the simulation boundary was set to 2.5 μm. In addition, a 4-μm SiO_2 substrate was modeled. That thickness was chosen considering the SOI wafer used for fabrication (the thickness of the SOI wafer before processing was 1 μm for the device layer, 4 μm for the SiO_2 layer, and 650 μm for the substrate).

When working with interlayers, it is convenient to define a transition boundary condition, because a discontinuity in the tangential electric field is clearly present [57]. Transition boundary conditions are characterized by:

$$\vec{J_{S1}} = \frac{\left(Z_S\vec{E_{T1}} - Z_T\vec{E_{T2}}\right)}{Z_S^2 - Z_T^2}, \vec{J_{S2}} = \frac{\left(Z_S\vec{E_{T2}} - Z_T\vec{E_{T1}}\right)}{Z_S^2 - Z_T^2} \quad (1)$$

$$Z_S = \frac{-j\omega\mu}{k}\frac{1}{tan(kd)}, Z_T = \frac{-j\omega\mu}{k}\frac{1}{sin(kd)},\ k = \omega\sqrt{(\varepsilon + (\sigma(j\omega)))\mu} \quad (2)$$

where μ (relative permeability), ε (relative permittivity), and σ (electrical conductivity) are all taken from SiN. $E_{T1,2}$ are the transversal components of the electric field, and k is the wavenumber. The transition boundary thickness (d) is computed as 1 Å.

A tetrahedral grid with a maximum-element size below λ/20 [58] was used to mesh the computational model. Thereafter, the electric field distribution was calculated assuming Maxwell's equations:

$$\vec{\nabla} \times \left(\vec{\nabla} \times \vec{E} \right) - k_0^2 \varepsilon_r \vec{E} = 0 \tag{3}$$

where E is the electric field and k_0 is the free-space wavenumber. Resolving this equation, we can obtain the effective refractive index given by:

$$n = \sqrt{\varepsilon_r \mu_r} \tag{4}$$

$$\underline{\varepsilon_r} = \varepsilon_r + \widetilde{\varepsilon}_r = \underline{n^2} = (n + i.\kappa)^2. \tag{5}$$

Due to the tolerance and robustness of the fabrication method, and based on previous papers [45], a working range of values was defined for the different WG dimensions (i.e., SiN and SiO_2 thickness). Therefore, WG widths and layer thicknesses were calculated, respectively, within the 0.5–20 μm and 50–500 nm size intervals.

A summary of the simulated model behavior is reported in Figure 3, where the effective refractive index (n_{eff}) of the guided fundamental single mode is plotted vs. the SiO_2 interlayer thickness. The SiO_2 thickness values below 50 nm were strongly affected by mesh size and computation errors. From the initial results, we observed that the waveguiding effectiveness dramatically increased for a SiO_2 thickness between 50 and 150 nm, when the WG is fabricated with more than three SiO_2 interlayers. Actually, a simulation of the model behavior for different WG widths was carried out.

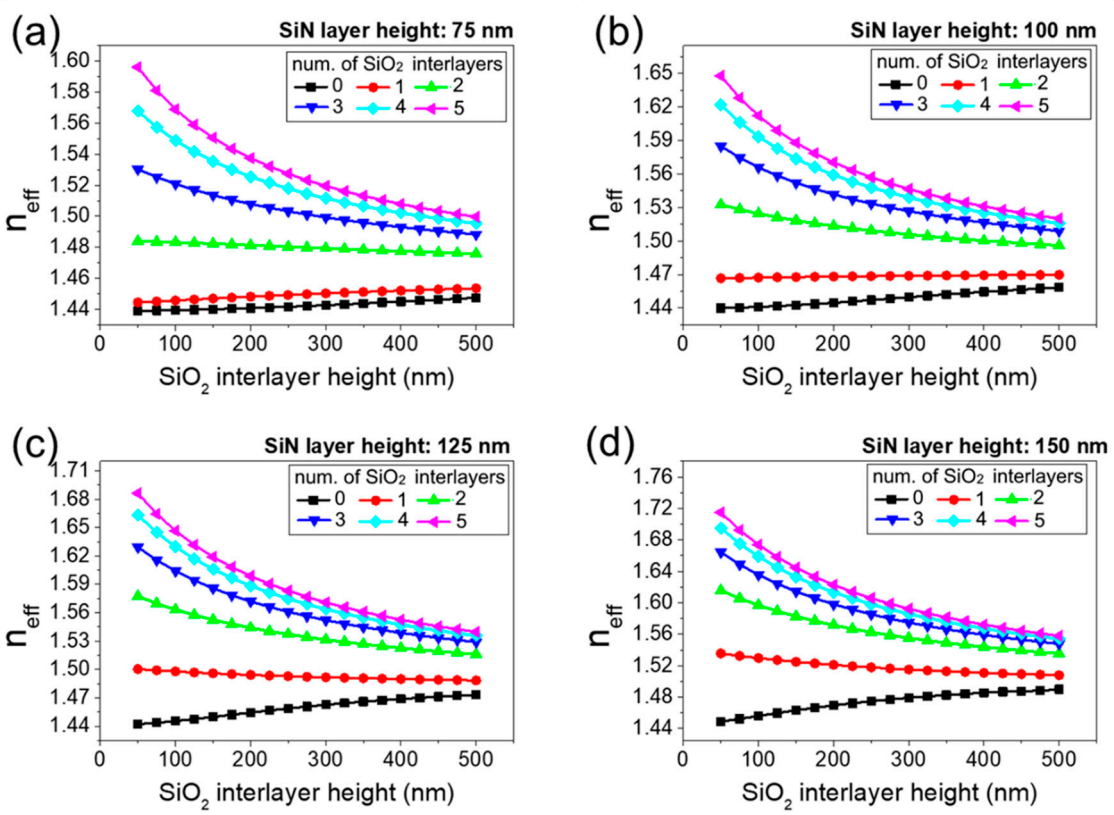

Figure 3. n_{eff} vs. SiO2 thickness at 1550 nm. Four SiN layer thicknesses: (**a**) 75 nm, (**b**) 100 nm, (**c**) 125 nm, and (**d**) 150 nm.

In Figure 4, a comparative study for the TM_{00} and TM_{01} modes at 1550 nm is plotted for a WG with three SiO_2 interlayers. In Figure 4a, a quasi-constant n_{eff} value for TM_{00} with WG widths above 4 μm can be observed. However, n_{eff} for TM_{01} becomes constant for WG widths above 10 μm. On the other hand, mode losses were calculated, as we show

in Figure 4b. As we can observe, for a reduced lateral dimension (below 3 μm) of the WG cross-section, light confinement is not possible along the WG (Figure 4a), and, therefore, the mode losses are significantly incremented as a result of the scattering losses increase (Figure 4b).

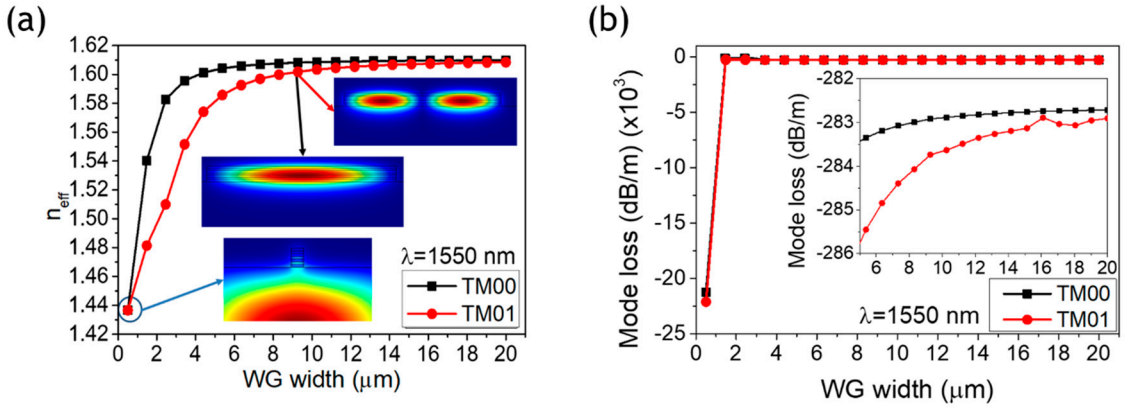

Figure 4. (**a**) n_{eff} vs. WG width for TM00 and TM01 is plotted. Inside the plot, different simulated profiles of the fundamental TM modes for a WG width of 9 μm at 1550 nm are shown. (**b**) Mode loss calculated for that range of WG widths is shown. The inset shows a zoom for the range of WG widths between 5 μm and 20 μm. These values were obtained for a multilayer WG with 3 SiO2 layers and 4 SiN layers.

In this context, we have simulated the cut-off wavelength for different interlayer numbers, as shown in Figure 5a.

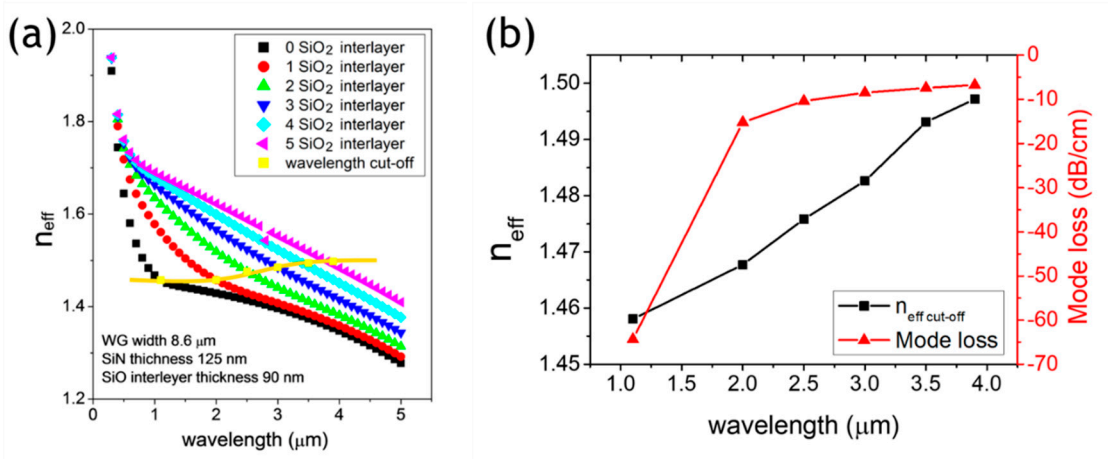

Figure 5. (**a**) n_{eff} vs. wavelength for different numbers of SiO_2 interlayers. The cut-off wavelength is also plotted in the graph (yellow curve) and in (**b**) n_{eff} at the cut-off wavelength and mode losses vs. wavelength are plotted.

Furthermore, in Figure 5b, the mode loss and the effective index at cut-off wavelengths are plotted. A dramatic increase in mode loss is observed with zero SiO_2 interlayers. When the number of interlayers is incremented, a similar mode loss (close to -5 dB/cm) may be obtained for three or more interlayers. These results demonstrate that a WG fabricated with three SiO_2 layers performs well for single mode guiding radiation at wavelengths from 1.5 μm to about 3 μm, which represents an ideal working range for our purposes.

The effective length (L_{eff}) was simulated in order to work in the regime where linear loss still dominates over non-linear loss. In that regime, TPA and TPA-induced free-carrier absorption (FCA) were not produced. The second process is because free-carriers that are excited to the conduction band could further absorb photons and be excited to higher

energy states. These carriers are distributed along the length of the device over the FCA effective length, $L_{FCA,eff}$:

$$L_{FCA,eff} = \frac{(1 - exp(-2\alpha_{lin}L))}{2\alpha_{lin}}. \quad (6)$$

The factor of two in the denominator is due to the dependence of free-carrier density on the square of the optical intensity.

As shown in Figures 3 and 4, an increment of n_{eff} occurs when we increment the number of SiO_2 interlayers. In order to understand the minimal number of SiO_2 interlayers to obtain a wide range of guided wavelengths, the propagation constant was calculated as a function of SiN and SiO_2 thickness for different numbers of layers (Figure 6). The propagation constant (also known as transmission constant) is the measure of the change in amplitude and phase per unit distance of the field vector. Calculations performed show an increment in the propagation constant given by the layer thickness increment (Figure 6a,b), whilst a reduction in the propagation constant is produced by incrementing the number of layers constituting the WG (Figure 6c).

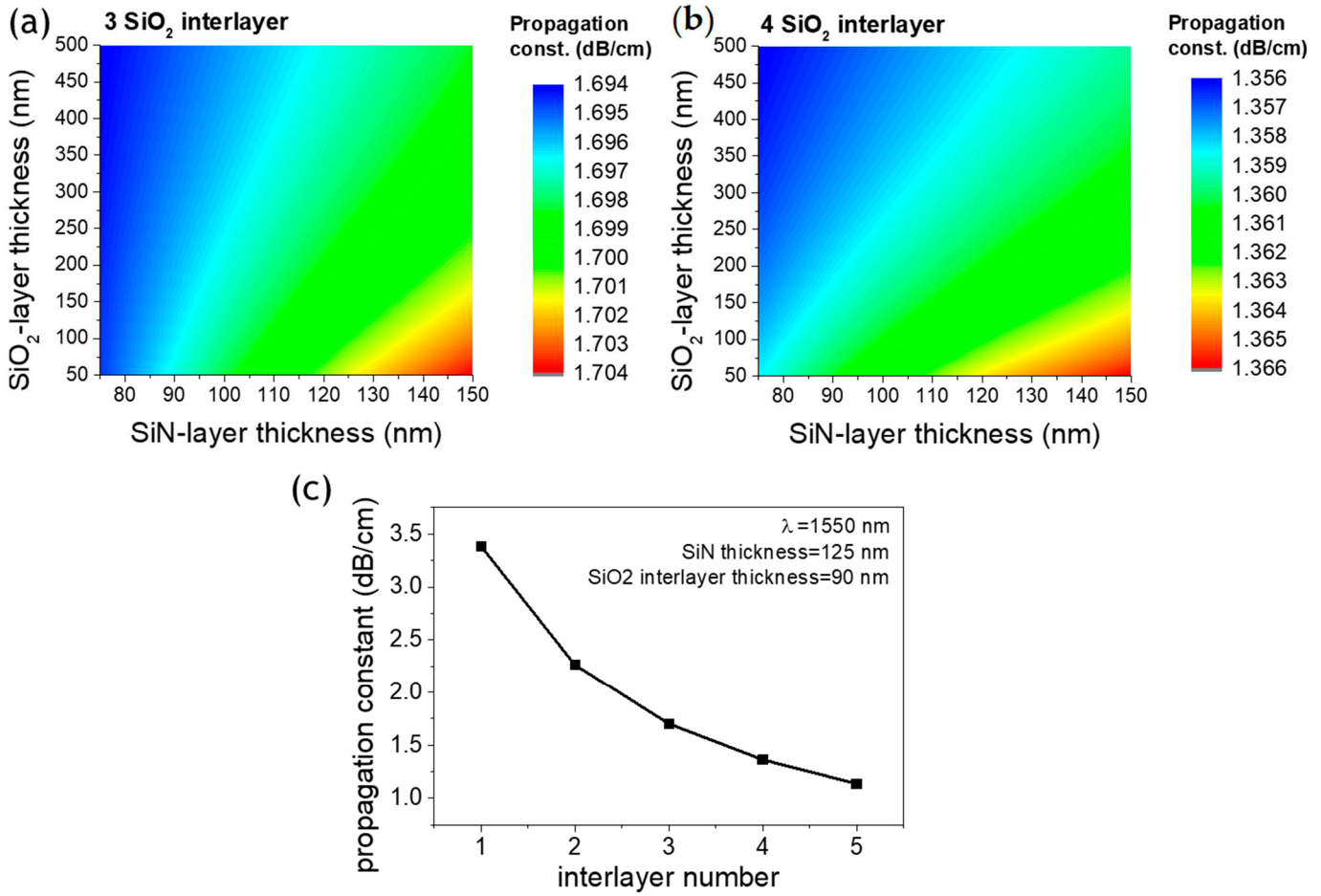

Figure 6. Propagation constant was plotted as function of SiO_2 and SiN thickness for (**a**) 3 SiO_2 interlayers and (**b**) 4 SiO_2 interlayers. (**c**) the propagation constant is given as a function of the number of interlayers. The layer thickness was fixed at 125 nm for SiN layers and at 90 nm for SiO_2 layers.

Figure 7a shows the effective length (L_{eff}) calculated for the cut-off refractive index for different numbers of interlayers. We can observe that L_{eff} differs from the linear behavior, (i.e., the FCA losses are higher). In particular, in Figure 7b, L_{eff} for three SiO_2 interlayers is plotted. L_{eff} of the device is a function of the physical length (L) and the linear loss (α_{lin}). In that regime, the linear loss still dominates over the non-linear loss and, thus, we can calculate the optimal WG length. We can note that above 6 mm, L_{eff} starts to draw away

from the linear behavior. That value for L_{eff} is similar to that shown by Motamedi et al. [30] (L_{eff} = 6 mm) for Si WGs. In their study, Si WGs had a dimension of 106 nm × 475 nm with a length equal to 14.9 mm and guided a fundamental TE mode at the 1500 nm wavelength. That result indicates that 6 mm is a good WG length for our purposes.

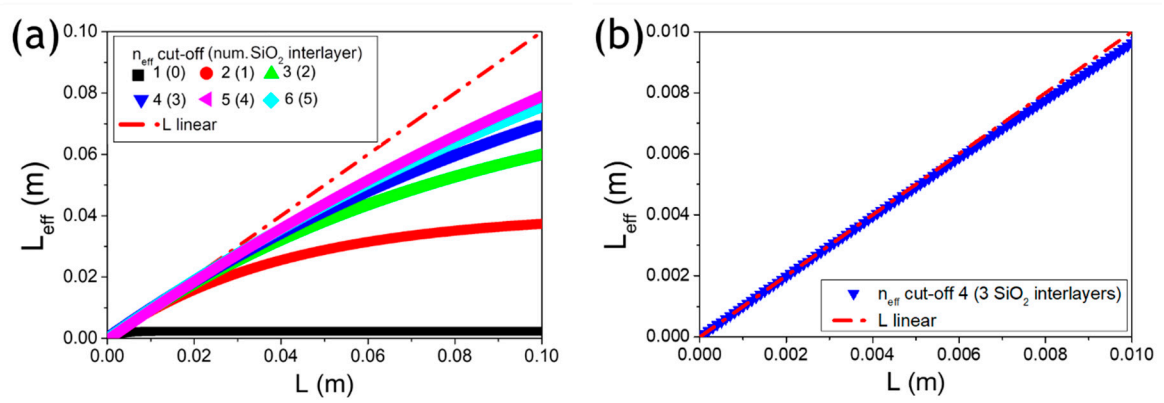

Figure 7. (**a**) Free-carrier absorption (FCA) effective length ($L_{FCA,eff}$) vs. WG length (L) for different numbers of SiO_2 interlayers. The linear behavior is also plotted in the graph (red dot) and (**b**) shows $L_{FCA,eff}$ for 3 SiO_2 interlayers below 10 mm.

Once we established the number of layers, we calculated the range of WG widths that offer less loss, as is shown in Figure 8. In Figure 8b, losses are plotted as a function of wavelength and WG width. In particular, for WG widths below 6 µm, a reduction in the range of guided wavelengths is obtained. As is shown in Figures 5a and 8a, for WGs fabricated with three SiO_2 interlayers, the cut-off wavelength is about 3.1 µm. This particular can be solved for WG widths wider than 6 µm (Figure 8b) to obtain a wider range of guided wavelengths (from 300 nm to 3.1 µm).

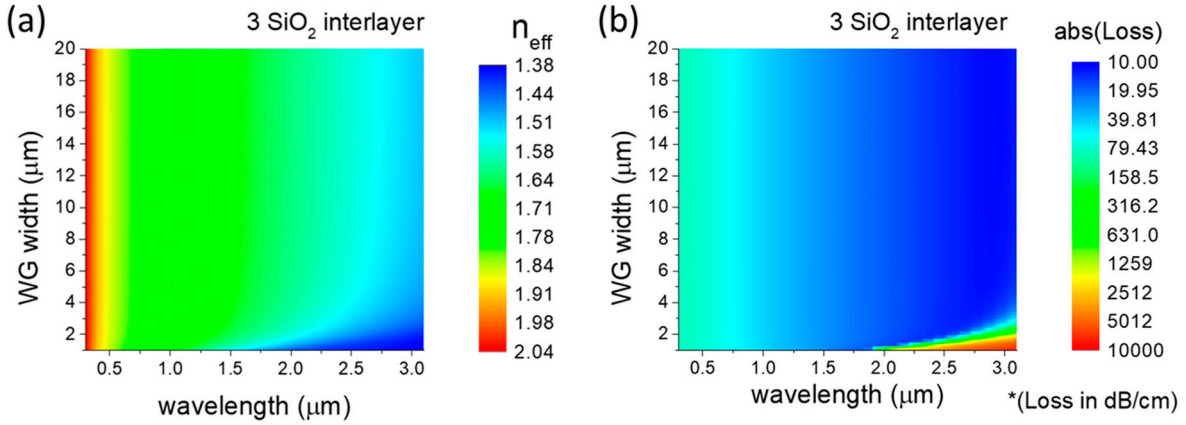

Figure 8. (**a**) Effective refractive index and (**b**) loss are plotted as a function of WG width and wavelength for 3 SiO_2 interlayers. The layer thickness was 125 nm for SiN layers and 90 nm for SiO_2 layers.

In order to perform an experimental test of the waveguiding behavior by using laser sources emitting in the visible and telecom wavelengths, we requested of the manufacturer five WGs with widths ranging between 7 and 10 µm.

For the 9.4 µm-width WG, we report in Figure 9 the simulation (left) of fundamental TE/TM modes for 1550 nm and 2640 nm.

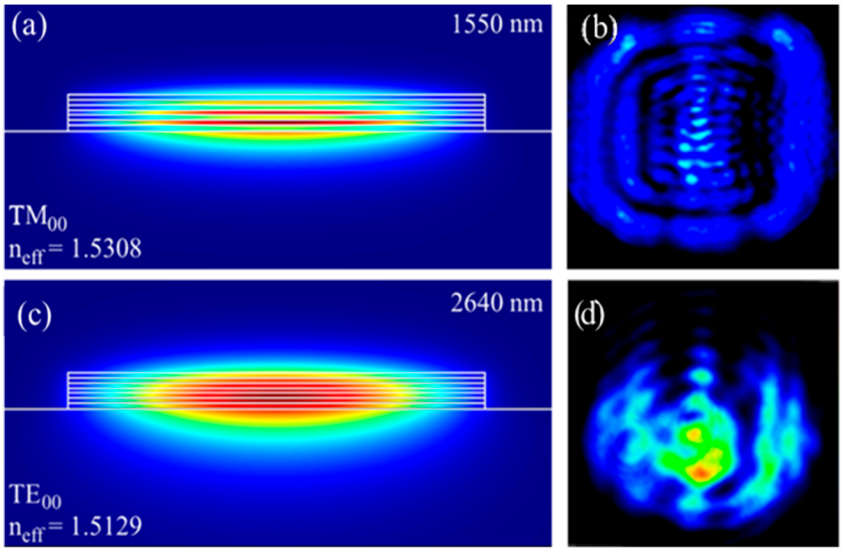

Figure 9. TEM mode calculations at different wavelengths for a WG of 9.4 μm width. The figure (**a**) shows the simulated TM mode at 1550 nm and figure (**c**) shows the simulated TE mode at 2640 nm. Figure (**b**,**d**) show the modes at 1550 nm and 2640 nm, respectively, obtained with an InSb camera for near infrared (NIR)/mid infrared (MIR) light.

A thorough WG characterization was performed by using the four lasers previously described. The inset of Figure 2 shows the WG behavior in the visible range, at 635 nm. All the light observed in the picture is solely due to a scattering process along the WG. Figure 9 (right) shows the NIR and MIR beam profiles guided through the WG, as recorded by the InSb camera. Such images, in agreement with the simulations (Figure 9 left), are a demonstration of single-mode waveguiding in the IR.

3.1.2. Finite Element Modeling for Stress Characterization

In order to get information on the local second-order non-linearity, a study of the behavior and influence of stress is necessary. Again, a stress evaluation across the multilayer WG cross section was made by using a FEM approach. We started this analysis from the previous analysis of Section 3.1.1.

The interlayer surface was defined with a surface load obtained according to the mass over the layer. A finer, free-triangular grid was employed to mesh the computational model. Deformation, stress, and strain at static equilibrium, in a stationary regime, were calculated assuming the following equations [59]:

$$\vec{F} + \vec{\nabla} \cdot \sigma = 0. \tag{7}$$

The total stress (σ) is given by:

$$\sigma = \sigma_{ad} + \vec{C} : \varepsilon_{el}, \varepsilon_{el} = \varepsilon - \varepsilon_{inel} \tag{8}$$

where the additional stress (σ_{ad}) is the sum of initial stress (σ_0), external stress (σ_{ext}), and q stress (σ_q):

$$\sigma_{ad} = \sigma_0 + \sigma_{ext} + \sigma_q. \tag{9}$$

The total strain contribution (ε) is established by the elastic (ε_{el}) and inelastic (ε_{inel}) strains. Inelastic strain (ε_{inel}) is given by the sum of initial strain (ε_0), thermal strain (ε_{th}), hygroscopic strain (ε_{hs}), plastic strain (ε_{pl}), and creep strain (ε_{cp}) [59].

$$\varepsilon_{inel} = \varepsilon_0 + \varepsilon_{th} + \varepsilon_{hs} + \varepsilon_{pl} + \varepsilon_{cr} \tag{10}$$

$$\varepsilon = \frac{1}{2}\left[\left(\nabla\vec{u}\right)^{T} + \nabla\vec{u}\right] \quad (11)$$

Figure 10 shows the color maps for the stress components σ_{xx} and σ_{yy} obtained from the equations. Several interesting features can be seen from the maps. In order to evaluate the stress-induced behavior, we simulated the stress profile along the x- and y-coordinates. In Figure 10c, it can be easily observed that the σ_{xx} component is not uniform along the y-coordinate; a critical increment is detected for SIN_y layers with relaxation behavior in SiO_2 layers introducing a stress gradient.

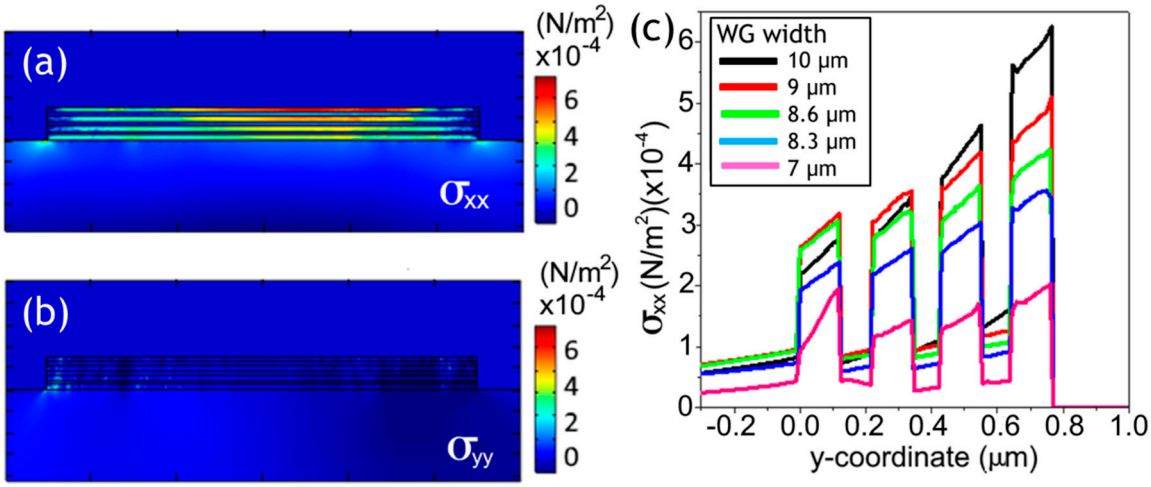

Figure 10. Stress calculations in a SiN multilayer WG with a width of 10 μm: (**a**) component σ_{xx} and (**b**) component σ_{yy}. Stress profile: (**c**) component σ_{xx} along the y-coordinate in x = 0.

3.2. Measurements

Using the setup described in Section 2.2, we realized a proof of principle test of WG loss in terms of transmitted power of some of the modeled structures on a large spectral range (from visible to MIR). In Figure 11, we report the average losses vs. the WG width of 6-mm-length SiN multilayer structures, for four different wavelengths. These values indicate that losses have a strong dependence on the wavelength of the propagating radiation and have a quasi-non-dependence on that range of WG widths, as expected. Moreover, from the measurements and from our FEM analysis, such WGs are demonstrated to work simultaneously in the NIR/MIR in single spatial mode.

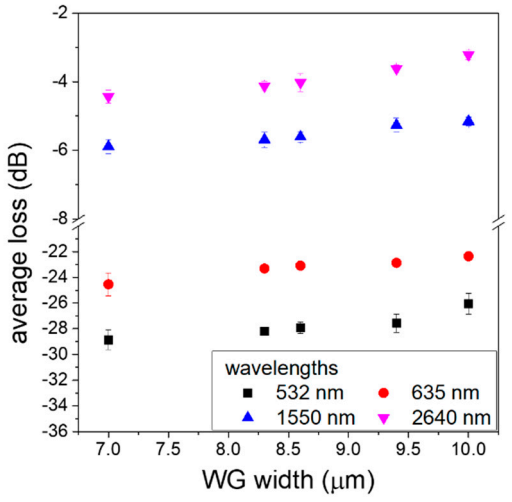

Figure 11. Coupling losses measured at 532 nm, 635 nm, 1550 nm, and 2640 nm for each WG width.

4. Discussion

In the IR range, losses are below 6 dB (measured at 1550 and 2640 nm), while, in the visible range, we observe an increment of about 20 dB (measured at 532 and 635 nm). Insertion losses are the sum of two contributions: propagation losses, probably due to different scattering processes along the WGs; coupling losses, due to spatial mode mismatch; and Fresnel reflections at input/output facets. Coupling losses cannot be easily estimated, due to the complexity of the WGs' geometry, preventing reliable numerical calculations. Nevertheless, we can set an upper limit for the coupling losses, assuming them to be equal to the coupling losses at 2640 nm, since at this longer wavelength, propagation losses are expected to be the lowest ones. As we indicate from the results obtained in Section 3.2, the lengths of the guides used in the test were below the effective length (6 mm), and, therefore, we assume that the propagation losses were negligible, and the losses measured are dueto coupling loss only. Losses measured at 1550 nm were close to those reported in other studies, as such 5.6 dB for Si WGs at 1500 nm with a 106 nm × 475 nm core [27] or 8 dB for SiN WGs at 1540 nm with a cross-section of 1.11 × 1.11 μm^2 [28].

Using FEM, we simulated different lengths for every WG and, consequently, we evaluated the propagation constant. In these calculations, the number of layers, the width, or the length could be fixed. In particular, considering 6-mm guides with three SiO_2 interlayers of different widths, a good agreement in terms of order of magnitude was obtained between simulation (Figure 8) and experimental evaluation of propagation losses (Figure 11). The measured values show a loss reduction at longer wavelengths. Furthermore, a slight increase in transmission for wider WGs was observed. Such increments are associated with better light coupling, due to the wider lateral dimensions.

Furthermore, as can be seen in Figures 7 and 11, this particular geometry, optimized for single-mode waveguiding between 1 and 3 μm, shows low losses and single-mode behavior also at shorter wavelengths, around 1.5 μm. This is due to a trade-off between the width of the guide, the number and thickness of the multilayers, and the scattering losses. The FEM simulations proved to be a very powerful tool to design this kind of photonic structure. Indeed, a careful modelling of multi-wavelength guides will enable modal phase-matching towards more efficient non-linear processes or for integrated photonic circuits useful in quantum optics, communication, spectroscopy, and sensing experiments operating simultaneously among NIR and MIR regions.

5. Conclusions

In this study, detailed theoretical modeling and experimental measurements were shown for novel silicon-based WG geometry. SiN multilayer structures were fabricated based on finite element modeling. At first, we fixed a set of parameters (wavelength and polarization) and performed simulations by varying interlayer height and WG width. The simulations show efficient single-mode waveguiding at wavelengths in the IR range (1.5–3 μm) for a WG made of 125-nm-thick SiN layers and 90-nm-thick SiO_2 layers. Furthermore, a stress simulation was performed, showing a stress gradient in the center of every WG. We characterized the waveguiding behavior in a wide range of wavelengths (532, 635, 1550, and 2640 nm). The WGs showed good waveguiding behavior at NIR–MIR wavelengths (both 1550 and 2640 nm, with loss values close to 4 dB), while losses increased at wavelengths in the visible range (about 20 dB). The losses measured for multilayer WGs were similar to those reported by other studies for Si or Si_3N_4 WGs [27,28]. Instead, from calculations, we did not observe any variation in loss values for different WG widths, because of minimal variations in the stress profile.

In addition, ZBLAN and chalcogenide glass are emerging as materials for MIR, particularly for fiber components. However, silicon technologies enable the realization of planar photonic circuits and devices (i.e., filters or resonators). The coupling, not simple in such a spectral region, could be improved by using precisely designed chalcogenide optical components.

In summary, we can conclude that Si_xN_y/SiO_2 multilayer WGs are good candidates for simultaneous MIR/NIR low-cost integrated optical components, providing broadband operation for spectroscopy and quantum technologies.

Author Contributions: For research articles I.L.G. performed the measurements, performed the numerical simulations, analyzed the data, and wrote the manuscript; M.S.d.C. contributed to the conception of the experiment, to the development of the experimental setup, and to simulation analysis; I.G. performed experimental measurements; P.C.P. and D.M. contributed to the conception of the experiment, to the simulations, and to the data interpretation; and P.D.N. contributed to the conception of the experiment and coordinated the experiment. All authors have read and agreed to the published version of the manuscript.

Funding: This research was funded by Provincia Autonoma di Trento, Grandi Progetti 2012 call, within the SiQuro project.

Institutional Review Board Statement: Not applicable.

Informed Consent Statement: Not applicable.

Data Availability Statement: The data presented in this study are available on request from the authors.

Acknowledgments: The authors wish to thank F. Ramirez-Manzano and M. Ghulinyan for the WG design and fabrication, and Lorenzo Pavesi, F. D'Amato, and S. Viciani for useful discussion.

Conflicts of Interest: The authors declare no conflict of interest.

References

1. Acín, A.; Bloch, I.; Buhrman, H.; Calarco, T.; Eichler, C.; Eisert, J.; Esteve, D.; Gisin, N.; Glaser, J.; Jelezko, F.; et al. The quantum technologies roadmap: A European community view. *New J. Phys.* **2018**, *20*, 080201. [CrossRef]
2. Riedel, M.F.; Binosi, D.; Thew, R.; Calarco, T. The European quantum technologies flagship programme. *Quantum Sci. Technol.* **2017**, *2*, 030501. [CrossRef]
3. The Future Is Quantum. Available online: https://www.qt.eu/ (accessed on 15 October 2020).
4. Dumke, R.; Lu, Z.; Close, J.; Robins, N.; Weis, A.; Mukherjee, M.; Birk, G.; Hufnagel, C.; Amico, L.; Boshier, M.G.; et al. Roadmap on quantum optical systems. *J. Opt.* **2016**, *18*, 093001. [CrossRef]
5. Korzh, B.; Ci Wen Lim, C.; Houlmann, R.; Gisin, N.; Jun Li, M.; Nolan, D.; Sanguinetti, B.; Thew, R.; Zbinden, H. Provably secure and practical quantum key distribution over 307 km of optical fibre. *Nat. Photonics* **2015**, *9*, 163–168. [CrossRef]
6. Caldwell, J.D.; Aharonovich, I.; Cassabois, G.; Edgar, J.H.; Gil, B.; Basov, D.N. Photonics with hexagonal boron nitride. *Nat. Rev. Mater.* **2019**, *4*, 552–567. [CrossRef]
7. Hoffman, A.; Gmachl, C. Extending opportunities. *Nat. Photonics* **2012**, *6*, 407. [CrossRef]
8. Borri, S.; Siciliani de Cumis, M.; Viciani, S.; D'Amato, F.; De Natale, P. Unveiling quantum-limited operation of interband cascade lasers. *APL Photonics* **2020**, *5*, 36101. [CrossRef]
9. Consolino, L.; Cappelli, F.; Siciliani de Cumis, M.; De Natale, P. QCL-based frequency metrology from the mid-infrared to the THz range: A review. *Nanophotonics* **2018**, *8*, 181–204. [CrossRef]
10. Galli, I.; Bartalini, S.; Ballerini, R.; Barucci, M.; Cancio, P.; De Pas, M.; Giusfredi, G.; Mazzotti, D.; Akikusa, N.; De Natale, P. Spectroscopic detection of radiocarbon dioxide at parts-per-quadrillion sensitivity. *Optica* **2016**, *3*, 385–388. [CrossRef]
11. Hao, Q.; Zhu, G.; Yang, S.; Yang, K.; Duan, T.; Xie, X.; Huang, K.; Zeng, H. Mid-infrared transmitter and receiver modules for free-space optical communication. *App. Opt.* **2017**, *56*, 2260–2264. [CrossRef]
12. Soibel, A.; Wright, M.; Farr, W.; Keo, S.; Hill, C.; Yang, R.Q.; Liu, H.C. Free space optical communication utilizing mid-infrared interband cascade laser. In *Free-Space Laser Communication Technologies XXII*; International Society for Optics and Photonics: Bellingham, WA, USA, 2010; Volume 7587, pp. 1–10. [CrossRef]
13. Hansen, M.G.; Magoulakis, E.; Chen, Q.-F.; Ernsting, I.; Schiller, S. Quantum cascade laser-based mid-IR frequency metrology system with ultra-narrow linewidth and $1 \times 10-13$-level frequency instability. *Opt. Lett.* **2015**, *40*, 2289–2292. [CrossRef] [PubMed]
14. Coluccelli, N.; Gambetta, A.; Cassinerio, M.; Laporta, P.; Galzerano, G. Mid-IR Solid-State Lasers for Spectroscopy and Metrology Applications. In Proceedings of the 2013 Conference on Lasers & Electro-Optics Europe & International Quantum Electronics Conference CLEO EUROPE/IQEC, Munich, Germany, 12–16 May 2013.
15. Tidemand-Lichtenberg, P.; Rodrigo, P.J.; Pedersen, C. Mid-Infrared Imaging using Up-conversion—Principles and Applications, in High-Brightness Sources and Light-driven Interactions. *Osa Tech. Dig.* **2018**. [CrossRef]
16. Ravaro, M.; Locatelli, M.; Pugliese, E.; Di Leo, I.; Siciliani de Cumis, M.; D'Amato, F.; Poggi, P.; Consolino, L.; Meucci, R.; Ferraro, P.; et al. Mid-infrared digital holography and holographic interferometry with a tunable quantum cascade laser. *Opt. Lett.* **2014**, *39*, 4843–4846. [CrossRef] [PubMed]

17. Li, C.; Liu, D.; Dai, D. Multimode silicon photonics. *Nanophotonics* **2018**, *8*, 227–247. [CrossRef]
18. Zou, Y.; Chakravarty, S.; Chung, C.-J.; Xu, X.; Chen, R.T. Mid-infrared silicon photonic waveguides and devices. *Photonics Res.* **2018**, *6*, 254–276. [CrossRef]
19. Borghi, M.; Castellan, C.; Signorini, S.; Trenti, A.; Pavesi, L. Nonlinear silicon photonics. *J. Opt.* **2017**, *19*, 093002. [CrossRef]
20. Lin, H.; Luo, Z.; Gu, T.; Kimerling, L.C.; Wada, K.; Agarwal, A.; Hu, J. Mid-infrared integrated photonics on silicon: A perspective. *Nanophotonics* **2018**, *7*, 393–420. [CrossRef]
21. Jalali, B. Nonlinear optics in the mid-infrared. *Nat. Photonics* **2010**, *4*, 506–508. [CrossRef]
22. Silverstone, J.W.; Bonneau, D.; O'Brien, J.L.; Thompson, M.G. Silicon Quantum Photonics. *IEEE J. Sel. Top. Quantum Electron.* **2016**, *22*, 6. [CrossRef]
23. Haas, J.; Mizaikoff, B. Advances in Mid-Infrared Spectroscopy for Chemical Analysis. *Ann. Rev. Anal. Chem.* **2016**, *9*, 45–68. [CrossRef]
24. Soler Penades, J.; Ortega-Moñux, A.; Nedeljkovic, M.; Wangüemert-Pérez, J.G.; Halir, R.; Khokhar, A.Z.; Alonso-Ramos, C.; Qu, Z.; Molina-Fernández, I.; Cheben, P.; et al. Suspended silicon mid-infrared waveguide devices with subwavelength grating metamaterial cladding. *Opt. Express* **2016**, *24*, 22908–22916. [CrossRef] [PubMed]
25. Sieger, M.; Mizaikoff, B. Optimizing the design of GaAs/AlGaAs thin-film waveguides for integrated mid-infrared sensors. *Photonics Res.* **2016**, *4*, 106–110. [CrossRef]
26. Hu, T.; Dong, B.; Luo, X.; Liow, T.-Y.; Song, J.; Lee, C.; Lo, G.-Q. Silicon photonic platforms for mid-infrared applications. *Photonics Res.* **2017**, *5*, 417. [CrossRef]
27. Motamedi, A.R.; Nejadmalayeri, A.H.; Khilo, A.; Kärtner, F.X.; Ippen, E.P. Ultrafast nonlinear optical studies of silicon nanowaveguides. *Opt. Express* **2012**, *20*, 4085–4101. [CrossRef] [PubMed]
28. Chang, L.; Pfeiffer, M.H.P.; Volet, N.; Zervas, M.; Peters, J.D.; Manganelli, C.L.; Stanton, E.J.; Li, Y.; Kippenberg, T.J.; Bower, J.E. Heterogeneous integration of lithium niobate and silicon nitride waveguides for wafer-scale photonic integrated circuits on silicon. *Opt. Lett.* **2017**, *42*, 803–806. [CrossRef]
29. Logan, D.F.; Giguere, M.; Villeneuve, A.; Helmy, A.S. Widely tunable mid-infrared generation via frequency conversion in semiconductor waveguides. *Opt. Lett.* **2013**, *38*, 4457–4460. [CrossRef]
30. Fujimura, M.; Okabe, H.; Beniya, K.; Suhara, T. Waveguide Quasi-Phase-Matched Sum-Frequency Generation Device Pumped by InGaAs Laser Diode for Single-Photon Detection in Communication Wavelength Band. *Jpn. J. Appl. Phys.* **2007**, *46*, 868. [CrossRef]
31. Bisadi, Z.; Mancinelli, M.; Manna, S.; Tondini, S.; Bernard, M.; Samusenko, A.; Ghulinyan, M.; Fontana, G.; Bettotti, P.; Ramiro-Manzano, F.; et al. Silicon nanocrystals for nonlinear optics and secure communications. *Phys. Stat. Sol. A* **2015**, *212*, 2659–2671. [CrossRef]
32. Tondini, S.; Castellan, C.; Mancinelli, M.; Kopp, C.; Pavesi, L. Methods for Low Crosstalk and Wavelength Tunability in Arrayed-Waveguide Grating for On-Silicon Optical Network. *J. Lightwave Technol.* **2017**, *35*, 5134–5141. [CrossRef]
33. Manna, S.; Ramiro-Manzano, F.; Ghulinyan, M.; Mancinelli, M.; Turri, F.; Pucker, G.; Pavesi, L. Multi-mode interference revealed by two photon absorption in silicon rich SiO_2 waveguides. *App. Phys. Lett.* **2015**, *106*, 071109. [CrossRef]
34. Manna, S.; Bernard, M.; Biasi, S.; Ramiro Manzano, F.; Mancinelli, M.; Ghulinyan, M.; Pucker, G.; Pavesi, L. Stimulated degenerate four-wave mixing in Si nanocrystal waveguides. *J. Opt.* **2016**, *18*, 075801. [CrossRef]
35. Signorini, S.; Mancinelli, M.; Borghi, M.; Bernard, M.; Ghulinyan, M.; Pucker, G.; Pavesi, L. Intermodal four-wave mixing in silicon waveguides. *Photonics Res.* **2018**, *6*, 805–814. [CrossRef]
36. Arahira, S.; Murai, H. Wavelength conversion of incoherent light by sum-frequency generation. *Opt. Express* **2014**, *22*, 12945–12961. [CrossRef] [PubMed]
37. Pecora, E.F.; Capretti, A.; Miano, G.; Dal Negro, L. Generation of second harmonic radiation from sub-stoichiometric silicon nitride thin films. *Appl. Phys. Lett.* **2013**, *102*, 141114. [CrossRef]
38. Khurgin, J.B.; Stievater, T.H.; Pruessner, M.W.; Rabinovich, W.S. On the origin of the second-order nonlinearity in strained Si–SiN structures. *J. Opt. Soc. Am. B* **2015**, *32*, 2494–2499. [CrossRef]
39. Avrutsky, I.; Soref, R. Phase-matched sum frequency generation in strained silicon waveguides using their second-order nonlinear optical susceptibility. *Opt. Express* **2011**, *19*, 21707–21716. [CrossRef]
40. Daldosso, N.; Melchiorri, M.; Riboli, F.; Girardini, M.; Pucker, G.; Crivellari, M.; Bellutti, P.; Lui, A.; Pavesi, L. Comparison Among Various Si_3N_4 Waveguide Geometries Grown Within a CMOS Fabrication Pilot Line. *J. Lightwave Technol.* **2004**, *22*, 1734. [CrossRef]
41. Levy, J.S.; Foster, M.A.; Gaeta, A.L.; Lipson, M. Harmonic generation in silicon nitride ring resonators. *Opt. Express* **2011**, *19*, 11415–11421. [CrossRef]
42. Ning, T.; Pietarinen, H.; Hyvärinen, O.; Simonen, J.; Genty, G.; Kauranen, M. Strong second-harmonic generation in silicon nitride films. *Appl. Phys. Lett.* **2012**, *100*, 161902. [CrossRef]
43. Gorin, A.; Jaouad, A.; Grondin, E.; Aimez, V.; Charette, P. Fabrication of silicon nitride waveguides for visible-light using PECVD: A study of the effect of plasma frequency on optical properties. *Opt. Express* **2008**, *16*, 13509–13516. [CrossRef]
44. Stefan, L.; Bernard, M.; Guider, R.; Pucker, G.; Pavesi, L.; Ghulinyan, M. Ultra-high-Q thin-silicon nitride strip-loaded ring resonators. *Opt. Lett.* **2015**, *40*, 3316–3319. [CrossRef] [PubMed]

45. Schriever, C.; Bianco, F.; Cazzanelli, M.; Ghulinyan, M.; Eisenschmidt, C.; de Boor, J.; Schmid, A.; Heitmann, J.; Pavesi, L.; Schilling, J. Second-Order Optical Nonlinearity in Silicon Waveguides: Inhomogeneous Stress and Interfaces. *Adv. Opt. Mater.* **2015**, *3*, 129–136. [CrossRef]
46. Cazzanelli, M.; Bianco, F.; Borga, E.; Pucker, G.; Ghulinyan, M.; Degoli, E.; Luppi, E.; Veniard, V.; Ossicini, S.; Modotto, D.; et al. Second-harmonic generation in silicon waveguides strained by silicon nitride. *Nat. Mater.* **2012**, *11*, 148–154. [CrossRef] [PubMed]
47. Mao, S.C.; Tao, S.H.; Xu, Y.L.; Sun, X.W.; Yu, M.B.; Lo, G.Q.; Kwong, D.L. Low propagation loss SiN optical waveguide prepared by optimal low-hydrogen module. *Opt. Express* **2008**, *16*, 20809–20816. [CrossRef] [PubMed]
48. Melchiorri, M.; Daldosso, N.; Sbrana, F.; Pavesi, L.; Pucker, G.; Kompocholis, C.; Bellutti, P.; Lui, A. Propagation losses of silicon nitride waveguides in the near-infrared range. *Appl. Phys. Lett.* **2005**, *86*, 121111. [CrossRef]
49. Wang, L.; Xie, W.; van Thourhout, D.; Zhang, Y.; Yu, H.; Wang, S. Nonlinear silicon nitride waveguides based on a PECVD deposition platform. *Opt. Express* **2018**, *26*, 9645–9654. [CrossRef]
50. Daldosso, N.; Melchiorri, M.; Riboli, F.; Sbrana, F.; Pavesi, L.; Pucker, G.; Kompocholis, C.; Crivellari, M.; Bellutti, P.; Lui, A. Low propagation loss SiN optical waveguide prepared by optimal low-hydrogen module. *Mater. Sci. Semicond. Proc.* **2004**, *7*, 453–458. [CrossRef]
51. Soman, A.; Antony, A. Broad range refractive index engineering of Si_xN_y and SiO_xN_y thin films and exploring their potential applications in crystalline silicon solar cells. *Mat. Chem. Phys.* **2017**, *197*, 181–191. [CrossRef]
52. Viciani, S.; Siciliani de Cumis, M.; Borri, S.; Patimisco, P.; Sampaolo, A.; Scamarcio, G.; De Natale, P.; D'Amato, F.; Spagnolo, V. A quartz-enhanced photoacoustic sensor for H_2S trace-gas detection at 2.6 μm. *Appl. Phys. B* **2015**, *119*, 21–27. [CrossRef]
53. Mancinelli, M.; Trenti, A.; Piccione, S.; Fontana, G.; Dam, J.S.; Tidemand-Lichtenberg, P.; Pedersen, C.; Pavesi, L. Mid-infrared coincidence measurements on twin photons at room temperature. *Nat. Commun.* **2017**, *8*, 15184. [CrossRef]
54. Sawaguchi, A.; Toda, K.; Nilhara, K. Mechanical and Electrical Properties of Silicon Nitride-Silicon Xarbide Nanocomposites Material. *J. Am. Ceram. Soc.* **1991**, *74*, 1142–1144. [CrossRef]
55. Luke, K.; Okawachi, Y.; Lamont, M.R.E.; Gaeta, A.L.; Lipson, M. Broadband mid-infrared frequency comb generation in a Si_3N_4 microresonator. *Opt. Lett.* **2015**, *40*, 4823–4826. [CrossRef] [PubMed]
56. Gao, L.; Lemarchand, F.; Lequime, M. Exploitation of multiple incidences spectrometric measurements for thin film reverse engineering. *Opt. Express* **2012**, *20*, 15734–15751. [CrossRef] [PubMed]
57. Jackson, J.D. Chapter2: Boundary-Value Problems in Electrostatic: I. In *Classical Electrodynamics*, 3rd ed.; John Wiley & Sons Inc.: Hoboken, NJ, USA, 1999; pp. 57–94.
58. Veronis, G.; Fan, S. Theoretical investigation of compact couplers between dielectric slab waveguides and two-dimensional metal-dielectric-metal plasmonic waveguides. *Opt. Express* **2007**, *15*, 1211–1221. [CrossRef]
59. Green, D.J. Chapter 2: Elastic behavior. In *An Introduction to the Mechanical Properties of Ceramics*; Cambridge University Press: Cambridge, UK, 2004; pp. 13–69.